INSTITUTE OF PHYSICS PUBLISHING JOURNAL OF PHYSICS D: APPLIED PHYSICS
J. Phys. D: Appl. Phys. 37 (2004) 185–199 PII: S0022-3727(04)61452-5

Modelling of radiation transfer in low temperature nanosecond laser-induced plasma of Al vapour

V I Mazhukin[1], V V Nossov[1], I Smurov[2] and G Flamant[3]

[1] Institute of Mathematical Modelling RAS, 125047, Miusskaya 4a, Moscow, Russia
[2] Ecole Nationale d'Ingénieurs de Saint-Etienne, 58 rue Jean Parot, F-42023 Saint-Etienne Cedex 2, France
[3] Institut de Science et de Génie des Matériaux et Procédés CNRS, BP 5 Odeillo 66125 Font-Romeu Cedex, France

Received 26 March 2003
Published 19 December 2003
Online at stacks.iop.org/JPhysD/37/185 (DOI: 10.1088/0022-3727/37/2/007)

Abstract
Gas-dynamical expansion and radiation transfer of Al vapour breakdown plasma induced by nanosecond laser action with an intensity of 10^9–2×10^{10} W cm^{-2} at the wavelengths of 1.06, 0.512, and 0.248 μm are modelled. Plasma evolution is described in the approximation of non-stationary radiative gas dynamics in the two-dimensional axially symmetrical formulation. Radiation transfer is found to exert a considerable effect on the evolution of the laser plasma. As the intensity increases, the radiative energy losses also increase, reaching 60% at 2×10^{10} W cm^{-2}, and cause the plasma temperature to be reduced proportionally. The energy escapes mainly through the side and, to a smaller extent, the frontal boundaries, the amount of energy escaping in the direction of the target being negligible. The dependence of plasma processes on the laser wavelength is due to specific features of the absorption mechanisms and the photo-absorption contribution under the action of visible and ultraviolet ranges of radiation. The spectral composition of the escaping radiation differs considerably from that of the equilibrium spectrum and is typical of plasma with a variable optical density. It is possible to take into account the influence of radiation on the plasma characteristics by solving the equation of radiation transfer in the multi-group approximation with several tens of spectral intervals. If the maximum available number of groups is used for selected spectrum intervals, the computational results can be compared to the experimental data of plasma emission.

1. Introduction

The action of focused laser radiation of sufficiently high intensity on a target causes its heating, melting and evaporation as well as the breakdown in a layer of evaporated matter and the formation of plasma [1–6]. The main characteristics of laser plasma (temperature, density, geometrical parameters, and optical thickness) vary significantly depending on the irradiation regime, first of all on intensity, pulse duration and radiation wavelength. The development of new types of lasers and laser-plasma techniques [7] have stimulated research in this field in recent years.

Studying the processes of radiation transfer is one of the most interesting and complex problems connected with describing the behaviour of laser plasma. As shown in [8], at temperatures not exceeding a few tens of eV and not too low plasma densities, the energy and pressure of the radiation are small compared to those of the matter. The effect of radiation on the energy balance and evolution of plasma is manifested in radiative energy losses. In addition, the intensity and spectral composition of escaping radiation can provide important information about plasma parameters [9–12].

Detailed studies of radiation transfer in plasma of ablation products under the action of laser irradiation in the milli- and

microsecond range was carried out in [4, 13–18]. In particular, it was shown in [13, 14] that radiation energy transfer plays a dominant role in the evolution of an Al vapour plasma under the action of microsecond laser pulses with an intensity of 10^8–10^9 W cm $^{-2}$, and radiative energy losses are 30–40% of the laser energy absorbed in the plasma. Also, it was established that radiative losses increase as the laser wavelength increases due to the higher temperature of the plasma [13, 16], and are reduced with a decrease in beam radius [16] due to the smaller thickness and effective emissivity of the plasma layer [18]. Plasma radiation transfer for the nanosecond duration case has been studied less extensively [19–22]. It was established in [19] that under the action of an ultraviolet (UV) laser with a pulse duration of 30 ns and radiation intensity of up to 10^9 W cm^{-2} the radiative energy losses of the plasma are as high as 35%. On the other hand, the authors of [23], investigating the plasma cloud structure under the action of UV radiation (the KrF laser) with an intensity of 10^8–10^9 W cm^{-2}, established that the plasma expansion is spherical and after the pulse termination is well described by the Sedov theory of shock waves that does not account for radiative losses. In [20] expansion and radiation transfer in the air plasma were investigated within the problem of laser shock processing (LSP) under the action of radiation pulses of 1.06 and 0.353 μm and an intensity of 4–17 GW cm^{-2}. In [21] radiation losses of the stationary plasma are estimated and the problems of inverse bremsstrahlung absorption and heating of the plasma are discussed. In [22] the coefficients of transmission and scattering are determined experimentally for a plasma layer under the action of the eximer laser with an energy density of 1–5 J cm $^{-2}$ on an Ni target, the energy transfer equation is solved numerically, which leads to conclusions as to the values of the plasma absorption coefficients, the scattering function and typical sizes of scattering centres.

Calculation of plasma radiation transfer involves considerable difficulties because the presence of a large number of elementary radiation processes and a complex charge composition lead to a strong dependence of radiation characteristics on the radiation frequency [8, 24–27]. The most serious computational difficulties are encountered when considering bond–bond transitions producing spectral lines. Therefore, to calculate the radiation field, approximate methods are employed that allow the spectrum integral characteristics—transmission, total radiation flux, radiative losses—to be determined with the required accuracy [8, 28]. In particular, to investigate plasma of variable optical density the multi-group approximation is widely applied. Within this approximation the whole frequency range in divided into several intervals (groups) and the average absorption coefficient is calculated for each group using, for example, the Planck or Rosseland averaging techniques. With this approach, the researcher has to solve a rather complicated question of how to divide the spectrum into groups and, particularly, how many spectral groups there should be. In the limiting case of one spectral group, the method is reduced to the known 'grey gas' approximation [8, 19]. In [4, 15] the radiation transfer is calculated using three spectral groups. In [17] six groups are used to approximate the absorption coefficient of air. In [29], to investigate x-ray radiation induced by laser plasma, the calculation involved 250 groups chosen on account of the special features of the continuous spectrum and the most prominent lines.

The correct calculation of the absorption coefficient for laser radiation is of great importance in modelling the interaction of laser radiation with plasma. In the IR frequency range (10.6, 1.06 μm) the interaction of laser radiation with metal vapour is quite well described by the bremsstrahlung absorption coefficient [19, 20, 30–32]. In [33, 34] to analyse the interaction of plasma with laser radiation the transmission coefficient was measured and then used to estimate the attenuation (extinction) coefficient. It was established that under the laser action at the wavelength $\lambda > 420$ nm the attenuation occurs due to the inverse bremsstrahlung absorption. For smaller wavelengths (in particular, for the KrF laser, $\lambda = 0.248$ nm), this approach leads to strongly underestimated values, which implies the presence of other absorption mechanisms. In [35, 36] the contribution of bond-free photo-transitions involving a laser quantum (photo-ionization) was taken into account. In [37] the collision–radiation model was applied to analyse the influence of photo-ionization and photo-excitation at the stage of laser plasma formation (optical breakdown) and it was shown that their contribution to absorption is dominant under the action of a UV laser. In [38] the absorption mechanisms of IR and UV laser radiation in erosion plasma are discussed, and the dominant role of photo-ionization in UV radiation/plasma interaction is underlined.

The main purpose of this study is to investigate the radiation transfer in Al vapour plasma in vacuum, induced by nanosecond laser irradiation with an intensity of 10^9–2×10^{10} W cm^{-2} and wavelengths of 1.06, 0.512 and 0.248 μm. Particular attention will be paid to the following: the effect of radiation on the principal characteristics of the plasma; the spatial distribution and spectral composition of the radiation flux escaping from the plasma; variation of the radiation contribution with decreasing wavelength; the effect of increasing the number of spectral groups on the accuracy of the multi-group approximation. Section 2 of this paper outlines the two-dimensional radiative gas dynamics (RGD) model and presents a detailed discussion of specific features of the absorption coefficients for the given plasma parameters and laser wavelength. Section 3 presents general characteristics of the process, the initial conditions are discussed, radiative losses are estimated, and the influence of the wavelength and the spectral peculiarities of the escaping radiation are studied. Discussion of the basic assumptions of the model and comparison with the experimental results are included in section 4. The main results of the work are summarized in the conclusion.

2. Formulation of the problem

The action on the target of the laser radiation of the range under consideration causes a rapid heating, melting and evaporation of the surface layer [5]. Interaction with the radiation leads to the breakdown of initially transparent vapour, the plasma produced starts absorbing the laser radiation and as a result the radiation has no access to the surface. Thus, the processes of evaporation, the breakdown on the one side and subsequent

evolution of the plasma appear to be separated to some extent. In this case the plasma can be investigated within the RGD approach by assuming that just above the target surface, at the initial instant of time, there is a motionless thin layer of plasma with the temperature $T = T_{\text{hot}}$ and density $\rho = \rho_{\text{hot}}$ [17, 20, 39].

2.1. *System of equations and boundary conditions*

The problem has axial symmetry and is solved in the cylindrical coordinate system introduced in the region above the target (figure 1). The z-axis coincides with the laser beam axis and is directed along the outer normal to the target surface. The plasma evolution is described with the following assumptions: (i) the plasma is an absorbing medium; (ii) the plasma is in the state of local thermo-dynamical equilibrium and satisfies the quasi-neutrality condition; (iii) evolution of the plasma is described in the approximation of a non-viscous non-thermo-conducting gas.

The plasma evolution is described by the complete system of equations for RGD supplemented by the laser radiation transfer equation and two equations of state [20, 39]:

$$\frac{\partial \rho}{\partial t} + \frac{1}{r}\frac{\partial}{\partial r}(r\rho u) + \frac{\partial}{\partial z}(\rho \upsilon) = 0 \tag{1}$$

$$\frac{\partial(\rho u)}{\partial t} + \frac{1}{r}\frac{\partial}{\partial r}(r\rho u^2) + \frac{\partial}{\partial z}(\rho u \upsilon) = -\frac{\partial(p+\omega)}{\partial r} \tag{2}$$

$$\frac{\partial(\rho \upsilon)}{\partial t} + \frac{1}{r}\frac{\partial}{\partial r}(r\rho u \upsilon) + \frac{\partial}{\partial z}(\rho \upsilon^2) = -\frac{\partial(p+\omega)}{\partial z} \tag{3}$$

$$\frac{\partial(\rho e)}{\partial t} + \frac{1}{r}\frac{\partial}{\partial r}(r\rho u e) + \frac{\partial}{\partial z}(\rho \upsilon e) = -p\left[\frac{1}{r}\frac{\partial(ru)}{\partial r} + \frac{\partial \upsilon}{\partial z}\right] - \left[\frac{1}{r}\frac{\partial q_r}{\partial r} + \frac{\partial q_z}{\partial z}\right] + \left[\frac{\partial G}{\partial z}\right] \tag{4}$$

$$\vec{\Omega}\,\text{grad}\, I_\nu + \kappa_\nu I_\nu = \kappa_\nu I_{\text{b}\nu}, \qquad \vec{q} = \int_0^\infty \partial\nu \int_{-1}^{1} I_\nu \mu\, \partial\mu \tag{5}$$

$$\frac{\partial G}{\partial z} - \kappa G = 0 \tag{6}$$

$$p = p(\rho, T) \tag{7}$$

$$e = e(\rho, T) \tag{8}$$

Here, t is the time, r and z the spatial coordinates, ρ the density, u and υ the velocity vector components, p the pressure, ω the artificial viscosity, e the specific internal energy, q_r and q_z the coordinates of the radiation flux vector, $\vec{\Omega}$ the unit vector of the direction of the photon, ν the frequency, I_ν and $I_{\text{b}\nu}$ the spectral intensities of the plasma radiation and the black body radiation, respectively, κ_ν and κ the absorption coefficients for thermal radiation and the laser radiation, respectively and G the laser radiation intensity. The three terms in square brackets in the energy balance equation (4) describe the work of pressure, the release of the energy of thermal radiation and that of laser radiation.

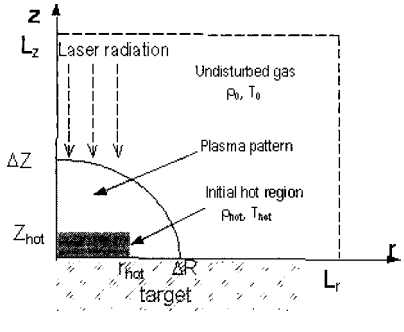

Figure 1. Problem set-up.

The system of equations is supplemented by the initial and boundary conditions:

$t = t_0$:

$$\begin{aligned} &u = \upsilon = 0, && 0 \leqslant (r \times z) \leqslant (L_r \times L_z) \\ &T = T_{\text{hot}}, \quad \rho = \rho_{\text{hot}}, && 0 \leqslant (r \times z) \leqslant (l_r \times l_z) \\ &T = T_0, \quad \rho = \rho_0, && (l_r \times l_z) < (r \times z) \leqslant (L_r \times L_z) \end{aligned} \tag{9}$$

$$r = 0: \qquad u = 0, \quad \frac{\partial \rho}{\partial r} = \frac{\partial \upsilon}{\partial r} = \frac{\partial P}{\partial r} = 0, \quad q_r = 0 \tag{10}$$

$$z = 0: \qquad \upsilon = 0, \quad \frac{\partial \rho}{\partial z} = \frac{\partial u}{\partial z} = \frac{\partial P}{\partial z} = 0, \quad cU = \sigma T^4 \tag{11}$$

$$r = L_r: \qquad p = p_0, \quad \rho = \rho_0, \quad u = \upsilon = 0, \quad q_r = -\frac{cU}{2} \tag{12}$$

$$z = L_z: \qquad p = p_0, \quad \rho = \rho_0, \quad u = \upsilon = 0, \quad q_z = -\frac{cU}{2}, \quad G = G_0 \tag{13}$$

where G_0 denotes the peak intensity of the laser pulse.

The tabular equations of state (7) and (8) calculated using the quantum-mechanical approach [40] are taken from [41]. The data cover the temperature range 0.025–100 eV (17 points) and the density range 10^{-6}–1 g cm^{-3} (eight points). The detailed consideration of the models for equations of state, the discussion of the applicability range and the comparison of the results for Al plasma are presented in [40, 42].

The main difficulty in solving the radiation transfer equation (5) is that its dimensionality is much greater than that of other equations, because the unknown function I_ν depends, in addition, on the variables $\vec{\Omega}$ and ν [8, 24, 39]. The problem can be simplified and the equation's dimensionality can be reduced with the help of the diffusion approximation (DA):

$$\begin{aligned} &\text{div}\,\vec{W}_\nu + c\kappa_\nu U_\nu = c\kappa_\nu U_{\text{b}\nu} \\ &\frac{c}{3}\,\text{grad}\, U_\nu + \kappa_\nu \vec{W}_\nu = 0 \end{aligned} \tag{14}$$

in which c is the speed of light and U_ν and $U_{\text{b}\nu}$ are the spectral energy density of radiation and equilibrium radiation, respectively:

$$U_{\text{b}\nu} = \frac{8\pi h \nu^3}{c^3(\exp(h\nu/kT) - 1)} \tag{15}$$

The frequency dependence of the functions $\kappa_\nu(\nu, \rho, T)$ and $U_\nu(\nu, \rho, T)$ is taken into account using the multi-group approximation: the entire frequency range is divided into a

finite number of intervals (groups), and the values of $\vec{q}$, U_ν, $U_{b\nu}$ are taken to be independent of frequency within each group,

$$\nu \in [\nu_{k-1}, \nu_k]: \qquad \vec{q}_\nu \equiv \vec{q}_k, \qquad U_\nu \equiv U_k,$$
$$U_{bk} = \int_{\nu_{k-1}}^{\nu_k} U_{b\nu}\,\mathrm{d}\nu; \quad [\nu_{\min}, \nu_{\max}] = \sum_{k=1}^{N} [\nu_{k-1}, \nu_k] \tag{16}$$

while the value of κ_ν is averaged using the Planck technique

$$\kappa_k = \frac{\int_{\nu_{k-1}}^{\nu_k} \kappa_\nu U_{b\nu}\,\mathrm{d}\nu}{\int_{\nu_{k-1}}^{\nu_k} U_{b\nu}\,\mathrm{d}\nu}$$

As a result, the initial equations (14) are transformed into a system of N equations independent of the variable ν:

$$\operatorname{div}\vec{q}_k + c\kappa_k U_k = c\kappa_k U_{bk}, \qquad k = 1, \ldots, N$$
$$\vec{q}_k = -\frac{c}{3\kappa_k}\operatorname{grad} U_k, \quad \vec{q} = (q_r, q_z) = \sum_{k=1}^{N}\vec{q}_k, \quad U = \sum_{k=1}^{N} U_k \tag{17}$$

The numerical solution of the problem is performed by the finite-difference method that is presented in detail in [17]. The algorithm consists of the main cycle on the time variable, and each time step includes three stages: (i) the solution of the radiation diffusion equation for each frequency group; (ii) the coupled solution of the averaged equation of the radiation diffusion and the energy equation; (iii) the solution of gas-dynamic equations.

2.2. *Plasma absorption coefficient*

The main mechanisms of quantum absorption in the plasma are connected with the free–free, bond–free (the continuous spectrum) and bond–bond (the discrete spectrum) transitions [8, 43]. Thus, the total absorption coefficient is written in the form of the sum

$$\kappa_\nu = \sum_i n_i \sigma_i^{\mathrm{bf}}(\nu) + \sum_{jk} n_j \sigma_{jk}^{\mathrm{bb}}(\nu) + \kappa_\nu^{\mathrm{ff}}$$

where n_i, n_j denote the populations of the electron levels in atoms and ions, σ_i^{bf}, $\sigma_{jk}^{\mathrm{bb}}$ are the absorption cross-sections for photo-ionization and photo-excitation, κ_ν^{ff} is the coefficient of bremsstrahlung absorption, and the summation is performed for all the processes permitted and accounted for in the given model. The photo-ionization cross-sections and the initial spectroscopic characteristics required for calculations (the ionization potentials, the energy levels, the oscillator strengths, the level lifetimes and some others) are found by solving the equation for the radial wave function of the electrons for all atoms and ions within the Hartree–Fock–Slater (HFS) model [25, 26, 44]. In some cases the calculated results are corrected using the reference data from the tables given in [45, 46]. The linear absorption cross-section $\sigma_{jk}^{\mathrm{bb}}$ is represented in the form of the product of the transition oscillator strength and the spectral line function. The line function is specified as having the Voigt shape, accounting for the thermal Doppler effect and electron impact broadening determined separately for neutrals and ions [25, 47]. For the coefficient of bremsstrahlung absorption in the ion field the following relation can be written [8]:

$$\kappa_\nu^{\mathrm{ff}} = \frac{8\pi e^6}{3mhc(6\pi mk)^{1/2}} \frac{n_e \sum_{z=1}^{Z_{\max}} z^2 n^z}{\nu^3 T^{1/2}} \left(1 - \exp\left(-\frac{h\nu}{T}\right)\right) \tag{18}$$

where n_e, n^z are the electron concentration and the total concentration of ions with charge z (the index $z = 0$ corresponds to a neutral atom); $Z_{\max}$ is the maximal ion charge accounted for in the model (for Al $Z_{\max} = 14$), h, m, and e are Planck's constant, the mass and the charge of the electron, respectively. The charge composition of the plasma for a given density and temperature is found from the condition for collision–radiation equilibrium (CRE) [25, 48, 49]. The collisional processes include electronic excitation, de-excitation and ionization, three-particle and dielectron recombination, the radiative processes include spontaneous radiative transitions between the levels and photo-recombination. At a high density of the plasma and a low temperature the results of calculations by the CRE model approximately coincide with the Saha–Boltzmann distribution, whereas at a low density and a high temperature the calculation results correspond to the coronal approximation.

On the diagrams presented in figures 2(*a*) and (*b*), several of the most prominent lines of the absorption coefficient at

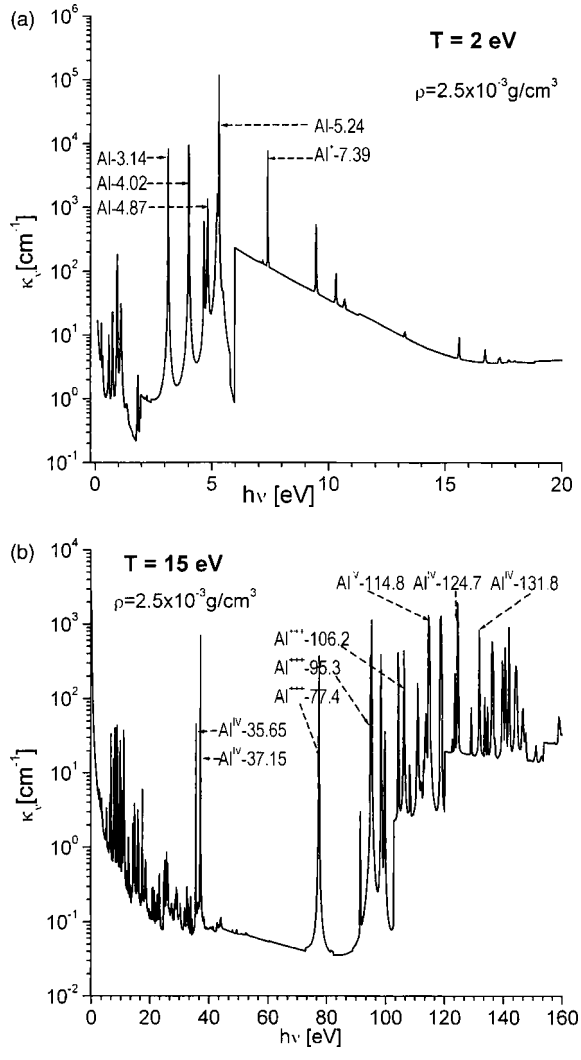

Figure 2. Linear absorption spectrum of Al plasma evaluated at (*a*) $T = 2$ eV and (*b*) $T = 15$ eV.

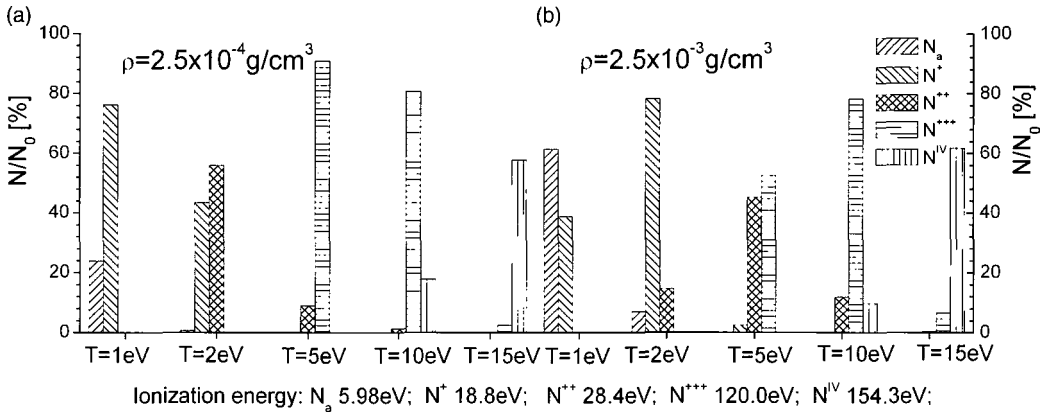

Figure 3. Charge composition of Al plasma evaluated at (*a*) $\rho = 2.5 \times 10^{-4}\,\mathrm{g\,cm^{-3}}$ ($N_0 = 5 \times 10^{18}\,\mathrm{cm^{-3}}$) and (*b*) $\rho = 2.5 \times 10^{-3}\,\mathrm{g\,cm^{-3}}$ ($N_0 = 5 \times 10^{19}\,\mathrm{cm^{-3}}$).

temperatures of 2 and 15 eV are shown. At a relatively low temperature (figure 2(*a*)), these are the lines of photo-transitions in a neutral atom and the first ion of Al. At the temperature of 15 eV (figure 2(*b*)), the most prominent lines are shifted into the short wavelength region and correspond to photo-transitions in the third and fourth ions. In order to explain the presence of particles with the ionization potentials of 120 and 154 eV in the plasma, let us consider how the charge composition of the plasma calculated by the CRE model varies as its temperature and density vary. In figure 3, the values of temperature $T = 1$, 2, 5, 10, and 15 eV are indicated on the x-axis (without complying with the scale). There are groups of columns crosshatched differently opposite each temperature value. The columns correspond to neutral N_a atoms and the N^+, N^{2+}, N^{3+}, N^{IV} ions. The height of each column is equal to the share of the given particles at a given temperature (the sum of the shares assigned to all the columns in the group equals 100%). The results presented in figure 3(*a*) were obtained at the plasma density of $2.5 \times 10^{-4}\,\mathrm{g\,cm^{-3}}$. At the temperature of 1 eV the singly charged ions constitute the main share (78%) of particles in the plasma. As the temperature rises to 2 eV the doubly charged ions become dominant, at 5 and 10 eV—the third ion, at 15 eV—the fourth ion. Such a dependence corresponds roughly to the Saha distribution, according to which at a low plasma density the ion with the given ionization potential J^z becomes dominant at a characteristic temperature of ~ 0.1–$0.2 J^z$ [49]. As the density rises, the plasma ionization degree is lowered (figure 3(*b*)). Thus, at the temperature of 2 eV it is not the second but the first ion that becomes dominant.

2.3. *Laser radiation absorption coefficient*

At a fixed radiation frequency equal to the laser frequency $\nu = \nu_l$, the HFS model makes it possible to determine the absorption coefficient for laser radiation. Figure 4 represents the temperature dependences of the absorption coefficient for the wavelengths $\lambda = 1.064$, 0.512, and 0.248 μm and the density $\rho = 2.5 \times 10^{-2}$ and $2.5 \times 10^{-3}\,\mathrm{g\,cm^{-3}}$.

For the region $T < 10$ eV, as the wavelength decreases, the behaviour of the absorption coefficient is explained by the increasing contribution of photo-absorption. For the radiation wavelength $\lambda = 0.512\,\mu$m (the quantum energy is $h\nu = 2.42$ eV), the bond–free transitions from the upper excited states of the atom become permitted, which

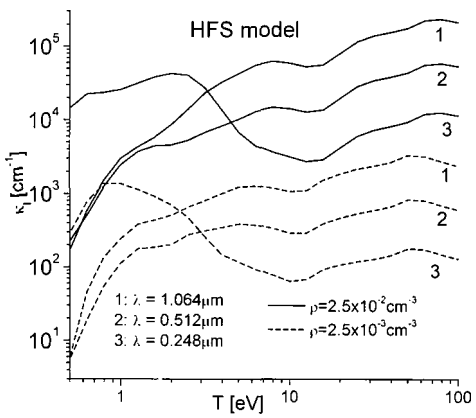

Figure 4. Absorption coefficients of laser radiation at wavelengths $\lambda = 1.064$, 0.512 and 0.248 μm, determined by the HFS model.

compensates the decrease in the bremsstrahlung effect, and the total absorption coefficient roughly coincides with the coefficient for $\lambda = 1.06\,\mu$m. At $\lambda = 0.248\,\mu$m the quantum energy is $h\nu = 5$ eV, which is only slightly smaller than the ionization potential of 5.98 eV for the Al atom. In this case photo-absorption becomes dominant and the value of the total coefficient becomes much greater than the value of the absorption coefficient for $\lambda = 1.06$ and 0.532 μm. In the temperature region $T > 10$ eV one can see the inverse cubic dependence of the absorption coefficient on the frequency and the quadratic dependence on the density. This indicates that the absorption coefficient is determined by the inverse bremsstrahlung effect. As shown above (figure 3), in the $T > 10$ eV temperature range the majority of particles are multi-charged ions and, owing to their energy structure, the probability of photo-transitions involving the laser quanta in question is very small.

The plots in figure 5 make it possible to compare the values of the absorption coefficient calculated by the HFS model that takes all possible ionization levels, $Z_{max} = 14$, into account and the results obtained using the model that accounts only for the bremsstrahlung absorption (18) and evaluated at a different number of ionized states, $Z_{max} = 3$ and 6 (the IB model). At temperatures below 10 eV the IB model gives quite accurate values for absorption at the wavelength of 1.06 μm (figure 5(*a*)), and the values are underestimated by several times for the visible range, $\lambda = 0.532\,\mu$m (figure 5(*b*)). For

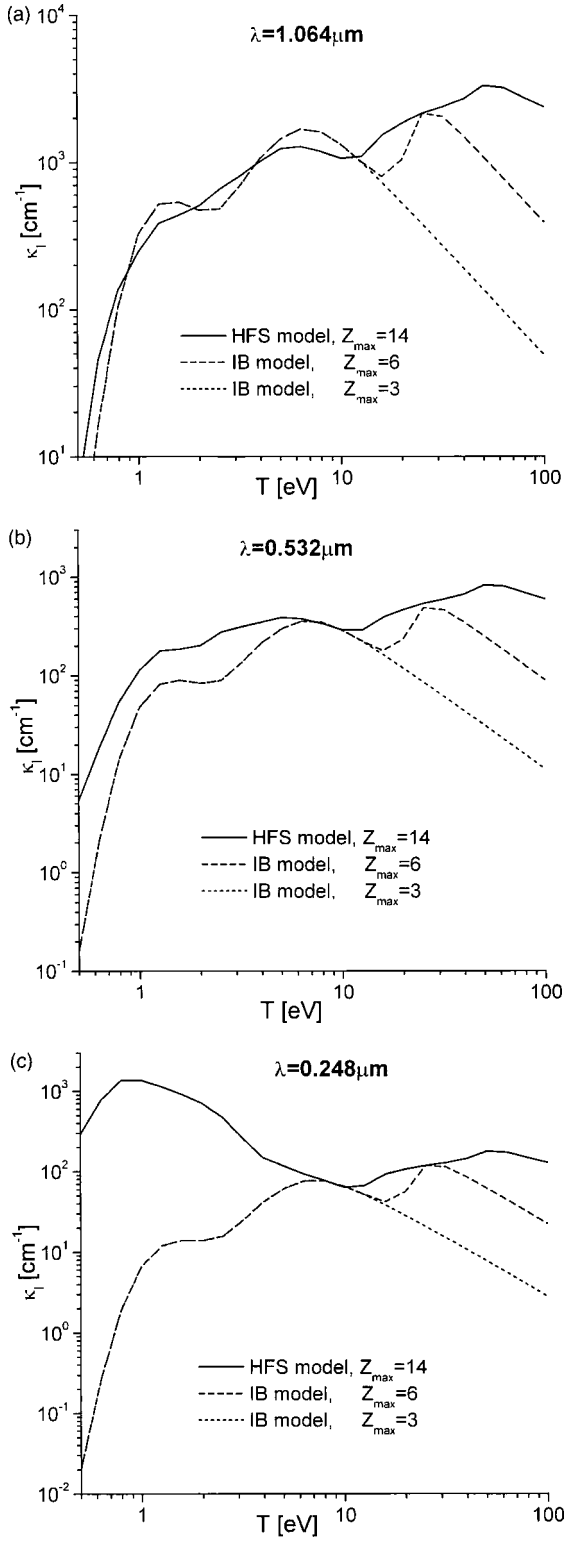

Figure 5. Comparison of absorption coefficients of laser radiation predicted by different models at wavelength (*a*) $\lambda = 1.064\,\mu$m, (*b*) $0.512\,\mu$m, and (*c*) $0.248\,\mu$m.

the UV radiation $\lambda = 0.248\,\mu$m (figure 5(*c*)), the deviation is as high as several orders of magnitude because photoabsorption plays the main role. As the temperature rises the results obtained using different models become closer. In the temperature region $T > 20$–30 eV, as the temperature rises, the bremsstrahlung absorption coefficient κ_ν^{ff} passes through a maximum and then decreases. The point at which the maximum is reached depends on the number of ions accounted for in the model—at this temperature all particles in the plasma are in the state of maximal ionization, the electron concentration reaches its limiting value, therefore at higher temperatures κ_ν^{ff} decreases as $\sim 1/T^3$ (18).

3. Analysis of modelling results

3.1. Modelling conditions and specification of the initial region

Let us analyse the influence of radiation transfer on the expansion of laser-induced Al vapour plasma in the following range of action parameters: the intensity $G_0 = 10^9$–$2 \times 10^{10}\,\mathrm{W\,cm^{-2}}$, the pulse duration $\tau = 10$ ns, the focusing spot radius $R = 0.025$ cm and the wavelengths of 1.06, 0.532 and $0.248\,\mu$m, which correspond to the Nd–YAG laser operating in the fundamental and doubled frequencies and the KrF laser, respectively. The spatial and temporal intensity distribution in the pulse was taken to be rectangular. The considered parameters correspond to the energy density $F = G_0 \times \tau = 10$–$200\,\mathrm{J\,cm^{-2}}$ and the total pulse energy $E = F \times \pi R^2 = 0.02$–$0.4$ J. The chosen regimes are considered by the authors of this paper to illustrate the effect of radiation transfer on the laser plasma and at the same time to be quite realistic. The lower limit of the laser intensity, $G_0 = 10^9\,\mathrm{W\,cm^{-2}}$, corresponds to the beginning of the 'high-irradiance regime' [6], and the upper limit, $G_0 = 2 \times 10^{10}\,\mathrm{W\,cm^{-2}}$, to the intensity used in LSP [50].

The parameters of the initial hot region $0 \leqslant (r \times z) \leqslant (r_{\mathrm{hot}} \times z_{\mathrm{hot}})$, $r_{\mathrm{hot}} = R$: the temperature $T = T_{\mathrm{hot}}$, the density $\rho = \rho_{\mathrm{hot}}$ and the thickness z_{hot} are specified by using experimental data and modelling results. According to [6], the thickness of the removed layer for plasma-dominated regimes of laser ablation in vacuum can be approximately predicted using the following relation: $X_{\mathrm{v}} \approx B(G_0\tau^{3/2}/\lambda)^{1/2}$. The experimental data on ablation of aluminium targets by nanosecond laser pulses were taken to evaluate the B constant [51–53]. The calculated X_{v} values for the action regimes considered in this paper are given in table 1.

Additional information on the parameters of the initial hot region have been obtained by modelling laser-induced evaporation in vacuum [54]. The model includes the non-linear heat transfer equation and the double-front variant of the Stefan problem describing melting and evaporation. The boundary conditions at the Knudsen layer have been formulated within the Crout approximation [54, 55]. The calculations have shown that the thickness of the vapour layer formed in a time of 10 ns is approximately $20\,\mu$m and is weakly dependent on the irradiation intensity. Setting $z_{\mathrm{hot}} = 20\,\mu$m, the density of the initial hot region is calculated to be $\rho_{\mathrm{hot}} = \rho_{\mathrm{Al}} \times X_{\mathrm{v}}/z_{\mathrm{hot}}$, $\rho_{\mathrm{Al}} = 2.7\,\mathrm{g\,cm^{-3}}$.

Much more uncertain is the estimation of the temperature T_{hot}. The principal reason is the lack of reliable data for the absorptivity of the target surface A_{sur} at high temperatures, which controls the intensity of the absorbed radiation $A_{\mathrm{sur}}G$. At room temperature the A_{sur} of pure aluminium is approximately 10% and is practically independent of radiation wavelength in the spectral range $\lambda \in [0.2$–$1]\,\mu$m [38, 56]. Modelling with the constant value of A_{sur} gives a steady-state vapour temperature $T_{\mathrm{vapour}} \approx 0.35$ eV at $G_0 = 10^9\,\mathrm{W\,cm^{-2}}$

Table 1. Estimated values of evaporated layer thickness X_v and initial hot region density ρ_{hot}.

Wavelength λ (μm)	1.06	1.06	1.06	0.53	0.248
Intensity G_0 (W cm^{-2})	10^9	5×10^9	2×10^{10}	5×10^9	5×10^9
Evaporated layer thickness X_v (μm)	0.22	0.38	0.75	0.53	0.75
Initial hot region density ρ_{hot} (g cm^{-3})	2.2×10^{-2}	5×10^{-2}	1×10^{-1}	7.2×10^{-2}	1×10^{-1}

and $T_{vapour} \approx 0.7$ eV at 10^{10} W cm^{-2}. If the increase of A_{sur} is accounted for being induced by the surface temperature rise and melt formation, the predicted T_{vapour} is 1.5–2 times higher. With the above results in mind the temperature of the initial hot layer is specified as $T_{hot} = 0.5$ eV and is not varied. More accurate specification of this parameter is possible by using some experimentally determined time-resolved characteristics of the plasma and accounting for the temporal shape of the laser pulse [20].

The remaining part of the computational domain ($r_{hot} \times z_{hot}$) $\leqslant$ ($r \times z$) $\leqslant$ ($L_r \times L_z$), $L_r = 5$ cm, $L_z = 25$ cm is initially filled with argon at the temperature $T_0 = 0.03$ eV and density $\rho_0 = 3 \times 10^{-6}$ g cm^{-3}, which corresponds to the pressure of $\approx 2 \times 10^{-3}$ bar. The role of the background gas will be commented on in section 4. The equation for radiation transfer was solved for the spectral range 0.1–200 eV, which was divided into groups in the following way: $h\nu \in$ [0.1–1] eV was one group, and for the remaining part of the range $h\nu \in$ [1.0–200] eV the logarithmic scale was used $h\nu_i \in [200^{(i-1)/N}, 200^{i/N}]$ eV, $i = 1, \ldots, N-1$, N is the number of groups taken in calculations to be equal to 7, 21, 61, 101 and 1001.

3.2. General characteristic of the process

Consider the specific feature of expansion of the plasma induced by the laser action at the wavelength of 1.06 μm, intensities of 10^9, 5×10^9, 2×10^{10} W cm^{-2} and the pulse duration of 10 ns (figures 6 and 7). Figure 6 shows the temperature distribution in plasma at the instant of pulse termination $t = 10$ ns. In all the cases the distributions are characterized by the presence of a hot region—the plasma core—with typical temperatures of 9 eV, 15 eV and 20 eV for three values of the intensity, respectively. The major part of the plasma pattern has a slightly lower temperature and the temperature decreases sharply at the boundaries of the plasma pattern. The figure also clearly shows the variation of the pattern shape as the intensity grows. At 10^9 W cm^{-2} the expansion in the axial and radial directions proceeds at almost the same velocities and at 2×10^{10} W cm^{-2} the plasma pattern is elongated along the z-axis. The typical velocity of the plasma axial expansion varies from 40 km s^{-1} at 10^9 W cm^{-2} to 150 km s^{-1} at 2×10^{10} W cm^{-2}. At a later instant of time $t = 50$ ns (figure 7), the plasma temperature decreases two times and the plasma pattern shapes are similar for the three cases, with the ratio of the axial to radial sizes being 2 : 1.

Figures 8 and 9 present the distributions of the density, velocity and radiation flux at the same instants for the laser action of 5×10^9 W cm^{-2}. The size and shape of the plasma pattern in the density diagram of figure 8(*a*) (the pulse termination time $t = 10$ ns) roughly correspond to the ones in the temperature diagram (figure 6(*b*)). The density decreases from $\sim 10^{-3}$ g cm^{-3} in the centre of the region to $\sim 10^{-5}$ g cm^{-3} close to the outer boundary. At a later instant of time $t = 50$ ns

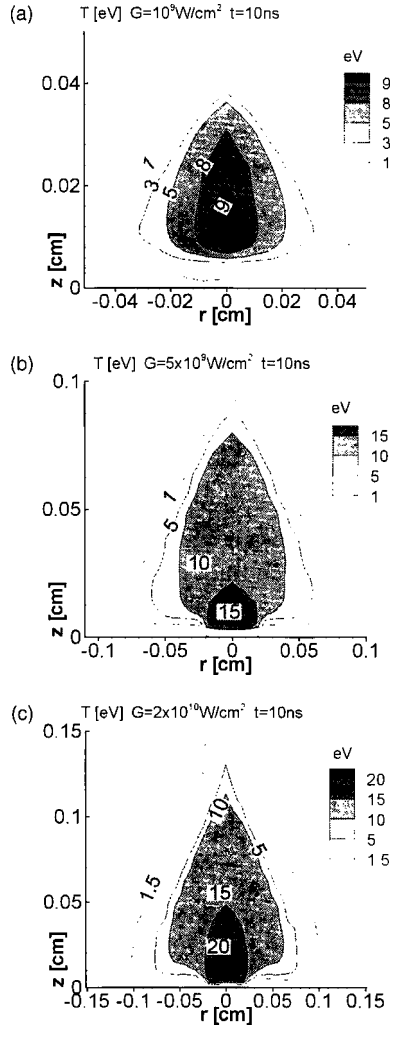

Figure 6. Plasma temperature distribution at laser intensity (*a*) $G_0 = 10^9$ W cm^{-2}, (*b*) 5×10^9 W cm^{-2} and (*c*) 2×10^{10} W cm^{-2}, $t = 10$ ns.

(figure 9(*a*)), the intensive expansion gives rise to a rarefaction zone inside the region. In this zone the density is lower than that of the background. The typical value of the velocity at the instant of 10 ns is 50 km s^{-1}, it is reached at the centre of the plasma pattern (figure 8(*b*)). Later the velocity is gradually reduced and at the instant of 50 ns it is 30 km s^{-1} (figure 9(*b*)). In contrast to the velocity, the typical value of the radiation flux (figures 8(*c*) and 9(*c*)), at the same period of time is reduced by three orders of magnitude, from 5×10^8 W cm^{-2} to 5×10^5 W cm^{-2}. The flux maximum is achieved not at the front but in a denser and cooler region close to the target, figure 8(*c*).

3.3. Influence of radiation transfer

Now, we consider how important the effect of radiation transfer is on the plasma evolution and, in particular, what number

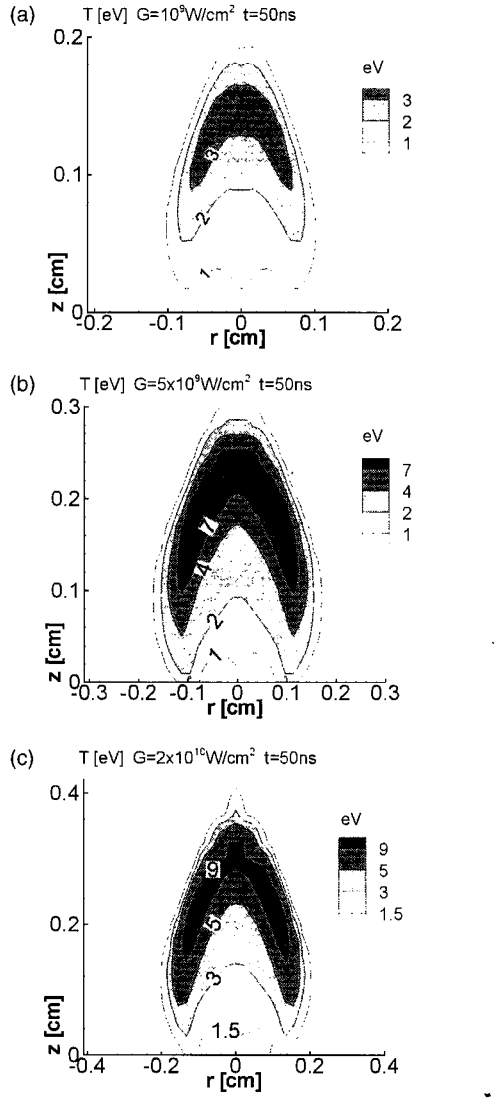

Figure 7. Plasma temperature distribution at laser intensity (*a*) $G_0 = 10^9\,\mathrm{W\,cm^{-2}}$, (*b*) $5 \times 10^9\,\mathrm{W\,cm^{-2}}$ and (*c*) $2 \times 10^{10}\,\mathrm{W\,cm^{-2}}$, $t = 50\,\mathrm{ns}$.

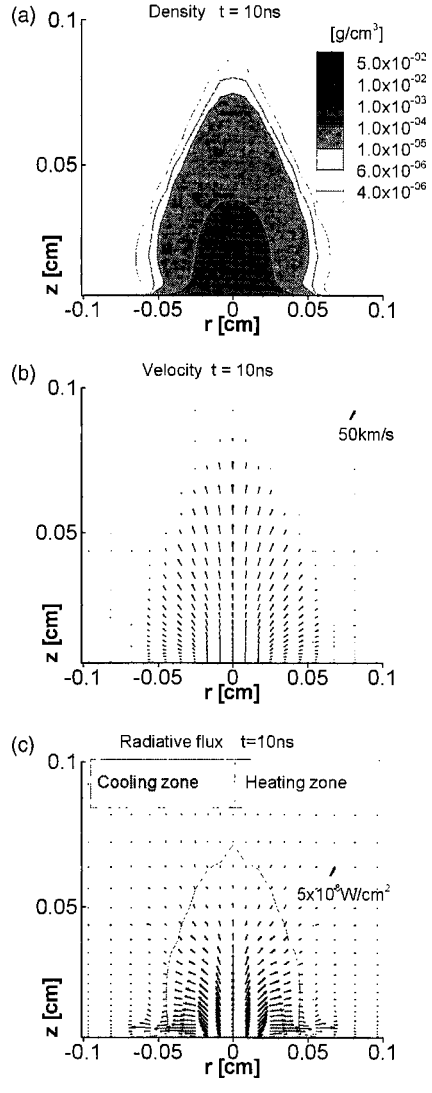

Figure 8. Distributions of (*a*) plasma density, (*b*) velocity and (*c*) thermal radiation flux at laser intensity $G_0 = 5 \times 10^9\,\mathrm{W\,cm^{-2}}$, $t = 10\,\mathrm{ns}$.

of groups allows us to calculate the plasma characteristics with sufficient accuracy when solving the radiation transfer equation within the multi-group approximation.

Figure 10 shows the dependences of the positions of the axial $\Delta Z(t)$ and radial $\Delta R(t)$ boundaries of the plasma for three different values of the intensity calculated using the model with the number of spectral groups being 7, 21 and without allowance for radiation. One can see that in the case when the radiation transfer is not considered and there are no radiative energy losses, the model gives overestimated values for the plasma sizes. The radiation grows in importance as the intensity rises and at $2 \times 10^{10}\,\mathrm{W\,cm^{-2}}$ the axial deviation is 15–20%. On the other hand, computations performed taking into account radiation transfer with seven and 21 spectral groups give practically the same results.

The dependences in figure 11 illustrate the effect of the radiation transfer on the plasma temperature. The plots $T(r = 0, z)$ on the beam axis for two instants of time 10 and 50 ns calculated with different numbers of spectral groups are given for three intensity values. Exclusion of radiation transfer leads to strongly overestimated values of temperature. The maximum deviation is achieved at $2 \times 10^{10}\,\mathrm{W\,cm^{-2}}$ and is $\approx$20 eV or 50%. In the course of time the absolute value of deviation decreases and the relative one is conserved. At the intensity of $10^9\,\mathrm{W\,cm^{-2}}$ the accurate temperature profile with respect to the number of groups can be obtained even with seven groups, whereas at a higher intensity 61 groups are required.

The diagrams in figure 12 show the total share of radiative losses $E_{\mathrm{emitted}}/E_{\mathrm{laser}}$ (the ratio of the energy removed by thermal radiation to the laser energy absorbed in the plasma) calculated for different numbers of groups. The major part of the energy is removed during the laser pulse action and the period $\sim\tau$ after termination of the pulse. As the intensity rises the radiative losses increase: from 10% at $10^9\,\mathrm{W\,cm^{-2}}$ (figure 12(*a*)) to 60% at $2 \times 10^{10}\,\mathrm{W\,cm^{-2}}$ (figure 12(*c*)). Computations with a small number of groups give overestimated values of the radiative energy removal. At the lowest intensity (figure 12(*a*)) the values of the ratio $E_{\mathrm{emitted}}/E_{\mathrm{laser}}$ calculated with seven and 101 groups differ by 20%. With increased intensity and, accordingly, the plasma temperature the dependence of the computational accuracy on the number of groups is smaller.

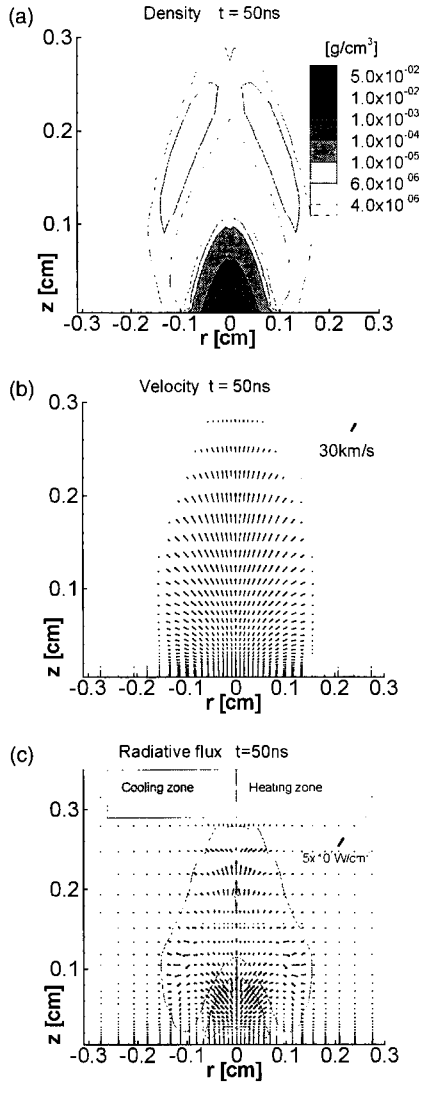

Figure 9. Distributions of (*a*) plasma density, (*b*) velocity and (*c*) thermal radiation flux at laser intensity $G_0 = 5 \times 10^9$ W cm^{-2}, $t = 50$ ns.

The dependences in figure 13 show the distribution of the energy removed by radiation in different directions. The major part of the energy is removed in the side direction and a smaller part in the frontal direction. The energy removal in the direction of the target is insignificant and its contribution does not exceed 1%.

3.4. Influence of radiation wavelength

We shall now analyse the plasma evolution under the action of laser radiation at three different wavelengths $\lambda = 1.06$, 0.532 and 0.248 μm. Several plasma characteristics taken at the beam axis $r = 0$ at $t = 5$ ns are shown in figure 14: (*a*) rate of energy release, (*b*) temperature and (*c*) density. Relations between these quantities for the action with 1.06 and 0.53 μm indicate that in these cases the radiation/plasma interaction is controlled by inverse bremsstrahlung absorption: the energy release rate, the temperature and the plasma size are greater for longer wavelength. For the action with 0.248 μm the photo-ionization gives an additional contribution to the interaction, which manifests itself as the maximum of div G and T at the

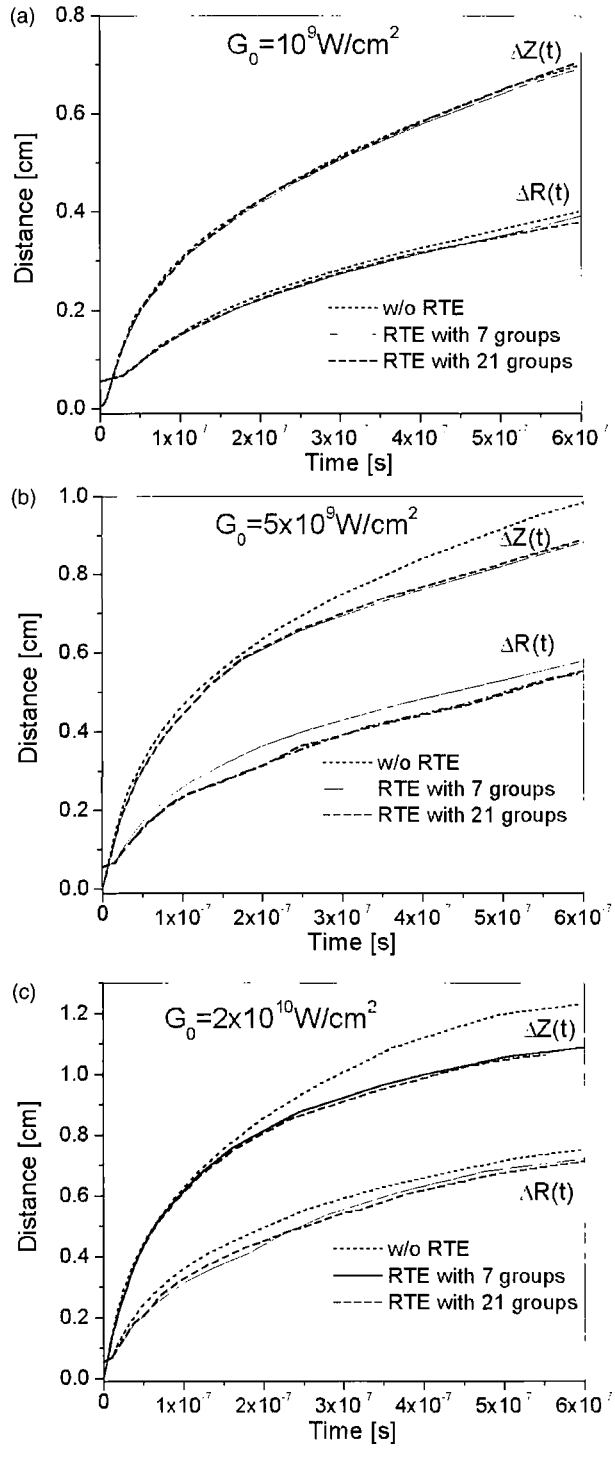

Figure 10. Coordinate of axial ΔZ and radial ΔR plasma boundaries determined by different models at laser intensity $G_0 = 10^9$, 5×10^9 and 2×10^{10} W cm^{-2}.

forefront of the plasma. The peculiarities of the profiles in the plasma centre result partially from different initial conditions.

The distributions of plasma temperature and density obtained make it possible, using the Saha formula, to calculate the electron concentration and to compare it with the critical concentration $N_{e.crit} = \pi m \nu^2 / e^2$, on reaching which the plasma becomes opaque and reflects the incident laser radiation. The values of $N_{e.crit}$ for the laser wavelengths under consideration are listed in table 2, where one can also find the computed maximum values for the electron concentration. It

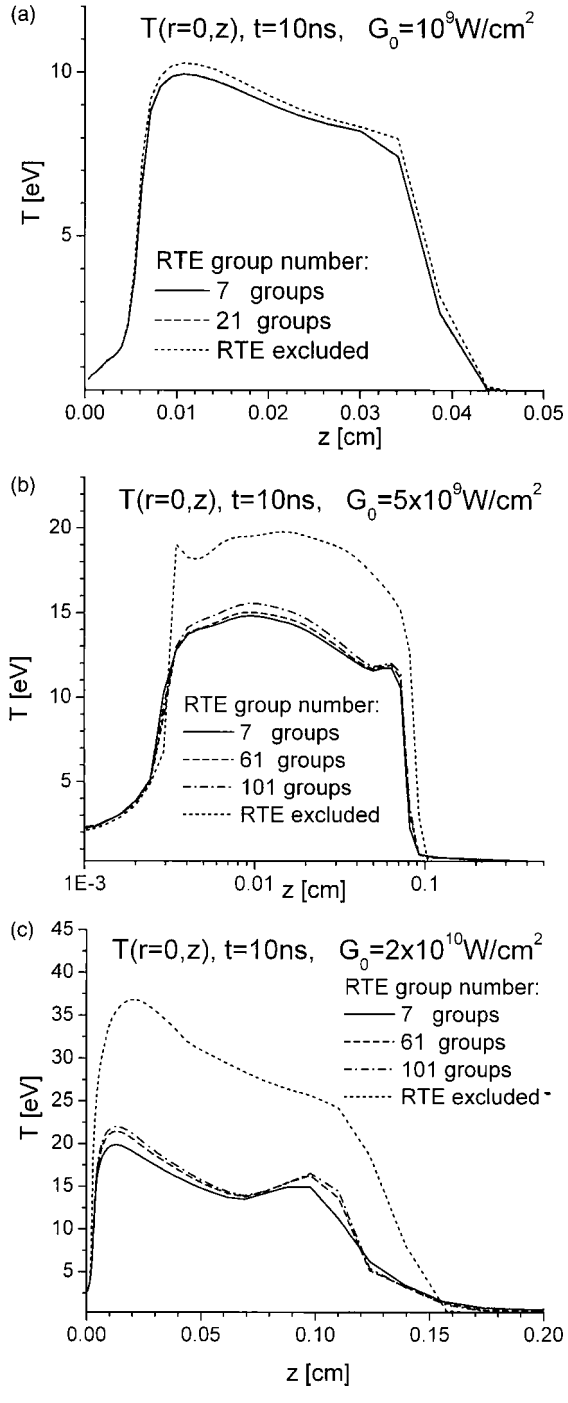

Figure 11. Plasma temperature plot at the beam axis at laser intensity (*a*) $G_0 = 10^9$, (*b*) 5×10^9 and (*c*) 2×10^{10} W cm^{-2}, $t = 10$ ns.

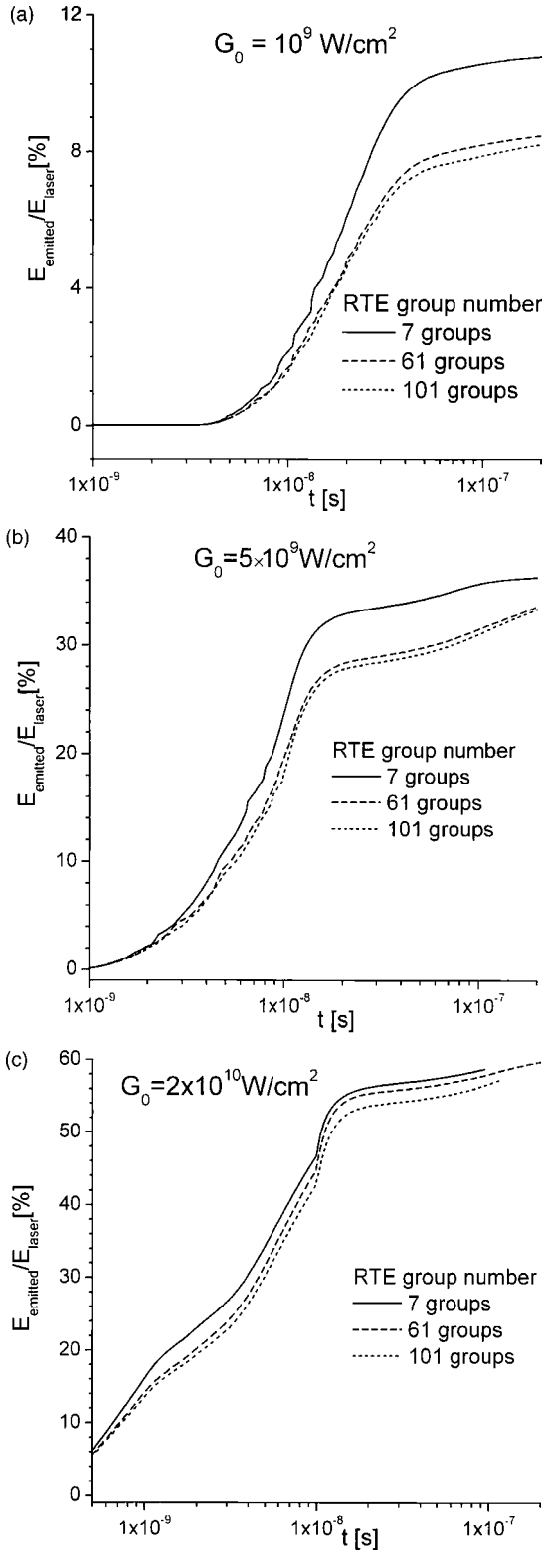

Figure 12. Total radiative energy losses predicted with different numbers of spectral groups at laser intensity (*a*) $G_0 = 10^9$, (*b*) 5×10^9 and (*c*) 2×10^{10} W cm^{-2}.

follows from the data presented that the concentrations of the order of critical ones can only be achieved under IR action with a wavelength of 1.06 μm and with the maximum (for this study) intensity. Even in this case, however, interaction of laser radiation with the plasma of 'above-critical' density does not occur, because the maximum values of concentration are achieved in the region in the vicinity of the target and the laser radiation is shielded at the plasma front where the concentration is much lower (figure 14).

In figure 15 one can see that lower temperatures of the plasma under the action of visible radiation with $\lambda = 0.532\,\mu$m and UV radiation with $\lambda = 0.248\,\mu$m are responsible for the fact that the radiative energy losses are reduced to 25% and 20%, respectively, as compared with the action of $\lambda = 1.06\,\mu$m. Additional calculations of these quantities for different numbers of groups showed that the results for 61 and 101 groups coincide with an accuracy of a few per cent.

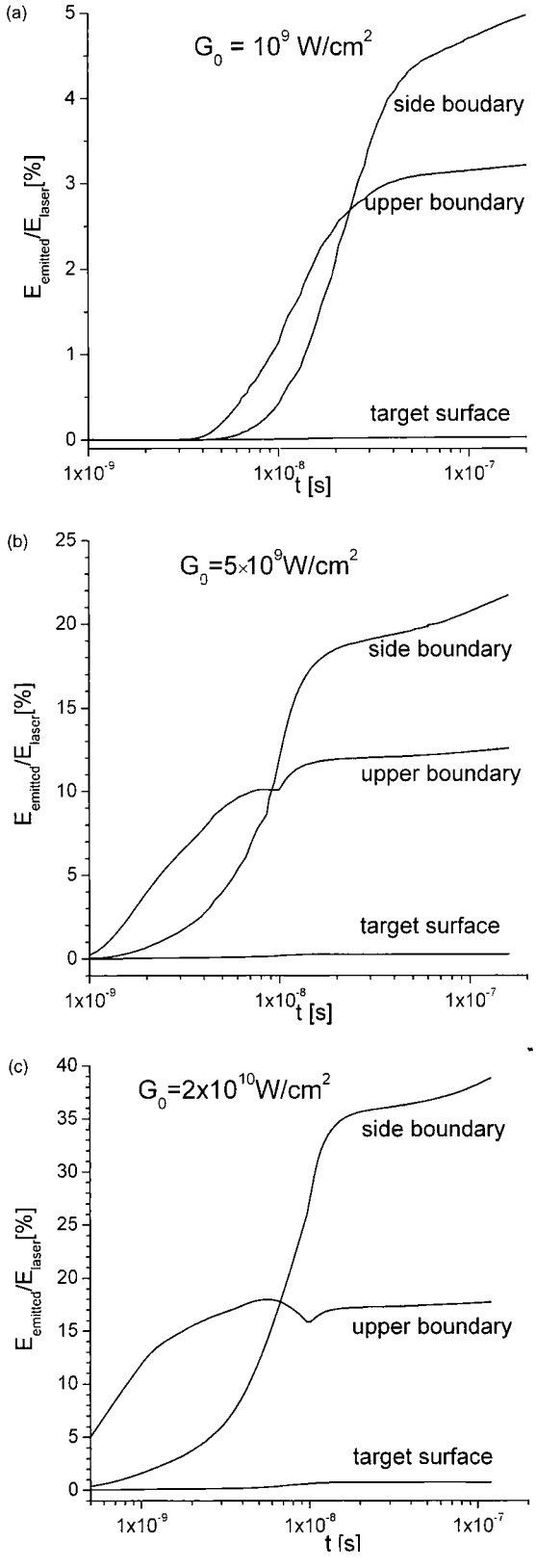

Figure 13. Radiative energy removal through the upper boundary, side boundary of the plasma pattern and the target surface at laser intensity (*a*) $G_0 = 10^9$, (*b*) 5×10^9 and (*c*) 2×10^{10} W cm^{-2}.

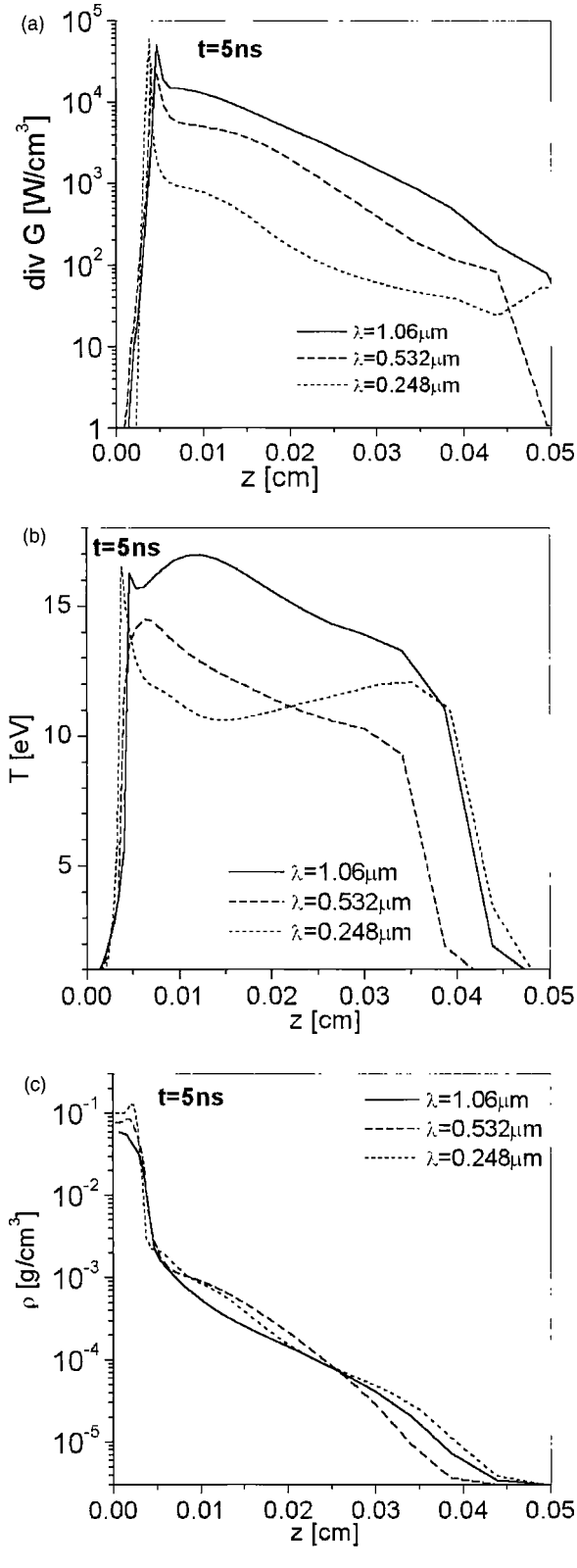

Figure 14. Plasma characteristics at the beam axis at laser wavelength $\lambda = 1.06$, 0.532 and 0.248 μm, $G_0 = 5 \times 10^9$ W cm^{-2}, $t = 5$ ns: (*a*) laser energy release rate div $G(z, r = 0)$, (*b*) temperature and (*c*) density.

3.5. Spectral characteristics of plasma

Figure 16 represents the spectral characteristics of the side radiation flux escaping from the plasma at $t = 10$ ns, as calculated under the action of $G_0 = 5 \times 10^9$ W cm^{-2}, $\lambda = 1.06\,\mu$m. The number of groups of the multi-group approximation was taken to be 21, 61, 101 and 1001. The most remarkable feature is the presence of a great number of lines in the spectra. As a consequence, the spectrum can be reproduced by only the most detailed spectral grid, as

Table 2. Comparison of critical electron concentrations and the maximal concentrations predicted in computations.

Wavelength (μm)	Electron concentration (cm^{-3})	
	Critical	Calculated maximum
1.06	9.8×10^{20}	6.0×10^{20} ($G_0 = 5 \times 10^9$ W cm^{-2}) 1.6×10^{21} ($G_0 = 2 \times 10^{10}$ W cm^{-2})
0.532	3.9×10^{21}	1.2×10^{21} ($G_0 = 5 \times 10^9$ W cm^{-2})
0.248	1.8×10^{22}	1.8×10^{21} ($G_0 = 5 \times 10^9$ W cm^{-2})

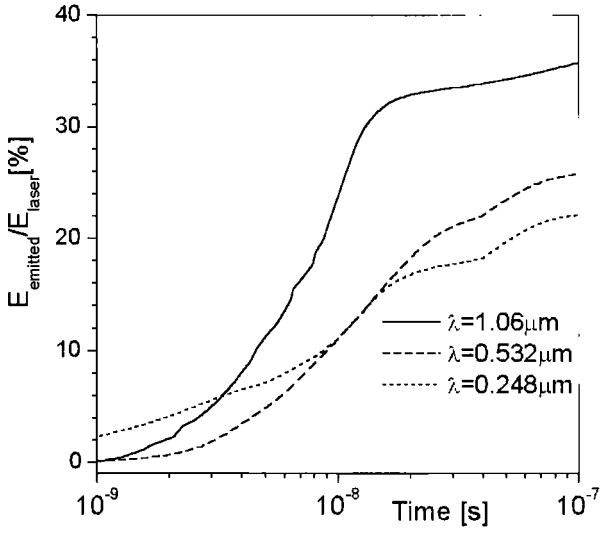

Figure 15. Total radiative energy losses at laser wavelength $\lambda = 1.06$, 0.532 and 0.248 μm.

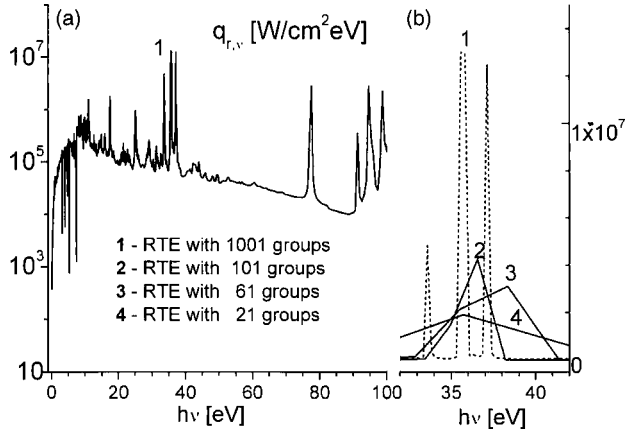

Figure 16. Spectral radiation heat flux at the side boundary at laser intensity $G_0 = 5 \times 10^9$ W cm^{-2}, $t = 10$ ns.

shown in figure 16(a). The plots for the narrower spectral range (figure 16(b)) clearly show that as the number of groups decreases, curves 2, 3, 4, the lines become indistinguishable and the predicted intensity of escaping radiation decreases inversely proportionally to the width of the spectral interval of the given group.

Typical values of plasma optical thickness are depicted in figure 17. The results are calculated for plasma parameters at the instant $t = 5$ ns: $T = 10$ eV, $\rho = 10^{-2}$ g cm^{-3} (plasma pattern centre), figure 17(a) and $T = 15$ eV, $\rho = 3 \times 10^{-4}$ g cm^{-3} (region at the distance of r_f from the surface) (figure 17(b)). As is seen (figure 17(a)), the plasma

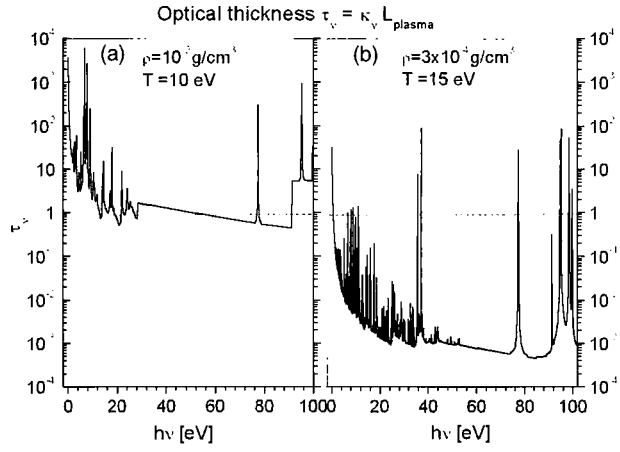

Figure 17. Optical thickness of the plasma evaluated at (a) $z = 4 \times 10^{-3}$ cm and (b) $z = r_f$, $L_{plasma} = 0.05$ cm.

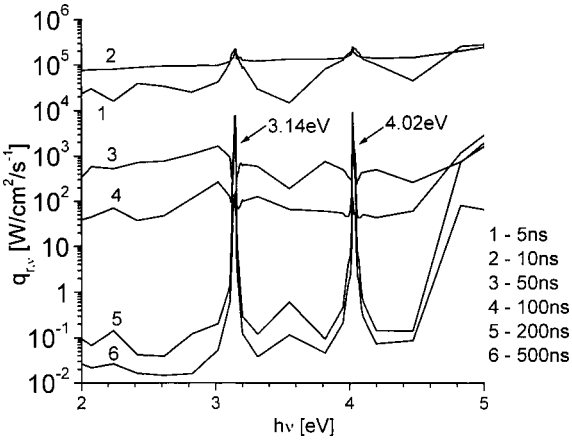

Figure 18. Evolution of spectral lines Al I (3.14 eV) and Al I (4.02 eV) of radiation heat flux at the side boundary at laser intensity $G_0 = 5 \times 10^9$ W cm^{-2}.

in the pattern centre is optically thick. Closer to the outer boundary the density decreases and the plasma becomes transparent in almost the entire spectral range (figure 17(b)).

In real plasma spectroscopy most observations are performed in a narrow spectral range lying in either the visible or UV parts of the spectrum 2–5 eV. The evolution of the strongest lines is followed in time and/or space; in the case of Al the strongest lines are Al I (3.14 eV) and Al I (4.02 eV) lines that correspond to the radiative decay of the first $4^2S_{1/2}$ and second $3^2D_{3/2,5/2}$ excited states of the neutral atom into the ground state $3^2P_{1/2,3/2}$. The spectral dependences of the radiation flux at the side boundary q_ν (figure 18), were computed for $G_0 = 5 \times 10^9$ W cm^{-2}, $\tau = 10$ ns using the spectral grid including 60 nodes logarithmically uniformly distributed plus 16 nodes in each of the 3.0–3.2 and 3.9–4.1 eV intervals, which provides the spectral resolution of 0.0125 eV. During the pulse, curves 1 and 2, the lines are practically indistinguishable or are strongly broadened. Starting from $t = 50$ ns the lines become visible, with the peak-to-background intensity ratio increasing with time. The line widths, curves 5 and 6, also increase with time, although the spectral resolution does not appear to be sufficient to represent this effect well enough.

4. Discussion and comparison with experiment

The results of this study show that the contribution of thermal radiation in the evolution of plasma induced by nanosecond laser radiation can be significant. At an intensity exceeding $5 \times 10^9\,\mathrm{W\,cm^{-2}}$, plasma radiation removes 30–60% of the laser energy accumulated in the plasma and redistributes it efficiently. In comparison with microsecond action [13] the effect of radiation manifests itself at higher laser intensity and plasma temperature. The differences are explained by the relatively small thickness of the radiative plasma layer $L_{\mathrm{plasma}} \sim 0.1\,\mathrm{cm}$ and fast density decrease caused by three-dimensional expansion [18]. The main parameter affected by radiation transfer is the plasma temperature. This fact can be additionally illustrated by the temporal dependence of the total internal E_{int} and kinetic E_{kin} energy of the plasma computed both with and without radiation transfer under the action of $G_0 = 5 \times 10^9\,\mathrm{W\,cm^{-2}}$, $\lambda = 1.06\,\mu\mathrm{m}$ (figure 19). Radiative energy transfer directly reduces the internal energy (the temperature), which leads to the reduction of pressure, the expansion slows down and kinetic energy decreases.

Calculations of energy transfer for different numbers of groups showed that it is possible to obtain accurate enough values of the main plasma characteristics using several tens of groups. A further increase in the number of groups does not give any practical advantage. On the other hand, the energy transfer should be taken into account over a sufficiently broad spectral range with the upper boundary $(h\nu)_{\max} \approx 10 \times T_{\mathrm{plasma}}$. If this condition is not fulfilled the value for the radiative energy transfer may be underestimated. For example, in the calculation for $G_0 = 2 \times 10^{10}\,\mathrm{W\,cm^{-2}}$, $\lambda = 1.06\,\mu\mathrm{m}$, assuming the upper limit of the spectral range $(h\nu)_{\max} = 100\,\mathrm{eV}$ instead of $(h\nu)_{\max} = 200\,\mathrm{eV}$, the total value for radiative losses turned out to be underestimated by about 25%.

Consider further the validity of assumptions used in the model. While analysing the plasma expansion in vacuum, one can distinguish two zones [6, 38]. The zone of hydrodynamic flow abuts the target surface and can be described in the continuum medium approximation. When the plasma density falls to an extent such that the mean free path of the plasma particles becomes comparable to the plasma size, the plasma enters the zone of inertial free-molecular expansion and can be analysed, for example, by means of direct statistical modelling. If a study is aimed at analysis of the hydrodynamic zone, the vacuum is substituted by a low-pressure medium, with the same equation of state as that of the vapour. In the case of Al vapour plasma, this approach corresponds to expansion in a low-pressure argon atmosphere [19, 31].

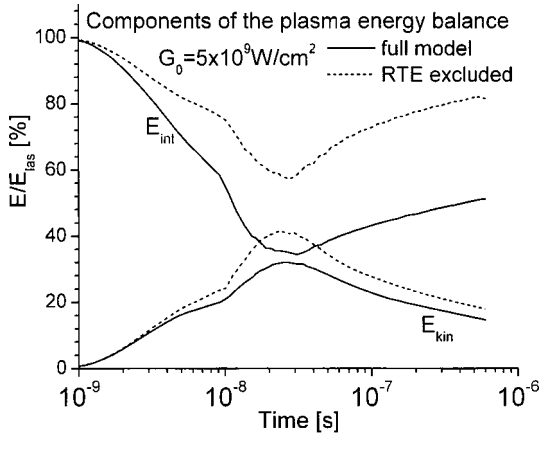

Figure 19. Influence of radiation transfer on internal (E_{int}) and kinetic (E_{kin}) energy of the plasma, at laser intensity $G_0 = 5 \times 10^9\,\mathrm{W\,cm^{-2}}$.

For the DA to be applicable for calculating the radiation transfer, the anisotropy of optical properties must be small, which is realized, in particular, in optically thick plasma [8, 24]. As follows from the results of section 3.5, this condition is fulfilled in the central region of the plasma plume. The powerful radiation flux formed here is partially reabsorbed and partially passes into the more rarified and optically thin boundary region of the plasma. According to the results of [8], the DA overestimates the attenuation rate of radiation flux in this 'configuration'; however, the quantitative error is not great at small optical distance from the radiation source. Another problem of DA application in an optically thin medium is the limitation of radiation flux that should not exceed the value of cU. In our study the flux limitation was implemented on the finite-difference level by respective approximation of $1/(\kappa_\nu \Delta z)$, $1/(\kappa_\nu \Delta r)$ coefficients of the flux.

The approximation of local thermodynamic equilibrium (LTE) is widely used in the analysis of erosion plasma. Its applicability depends primarily on the electron–ion relaxation time, which is the time needed for the electron gas to transfer the absorbed laser energy to heavy particles through elastic collisions [8]:

$$\tau_{\mathrm{ei}} = \frac{3.15 \times 10^8 A_{\mathrm{M}} T[\mathrm{eV}]^{3/2}}{Z\, N[\mathrm{cm^{-3}}] \times \ln \Lambda}$$

where $A_{\mathrm{M}}(=27)$ is the atomic weight, Z the degree of ionization, $\ln \Lambda$ denotes the Coulomb logarithm and N is the concentration of particles. Taking $T = 10\,\mathrm{eV}$ and $Z = 3$, one obtains that the relaxation time is shorter than the pulse duration at a density of $\sim 10^{-4}\,\mathrm{g\,cm^{-3}}$ ($N \sim 2.3 \times 10^{18}\,\mathrm{cm^{-3}}$) or higher. Thus, plasma non-equilibrium can manifest itself in the region near the plume boundaries.

For the purpose of additional verification the plasma was modelled for the same conditions as those in [59, 60]. In [59] the authors analysed experimentally the Al vapour plasma in vacuum, the plasma was induced by the laser action with $\lambda = 1.06\,\mu\mathrm{m}$, the intensity $G_0 = 3 \times 10^8\,\mathrm{W\,cm^{-2}}$ with an asymmetrical shape of the pulse, the pulse duration at half-maximum $\tau = 120\,\mathrm{ns}$ and a spot diameter of $150\,\mu\mathrm{m}$. The temperature and electron density of the plasma were determined by analysing the plasma emission spectrum, the lines of the Al first and second ions being considered separately. The dashed line in figure 20 shows the plasma temperature $T_{\mathrm{exp}}(\mathrm{Al}^{++})$ as obtained in the experiment and averaged over the plasma domain. The maximum value is reached at the pulse peak; then, the temperature rapidly decreases during a period of the order of the pulse duration. The average calculated temperature of the plasma $T_{\mathrm{av.l}}(t) = \sum_i (T_i \Delta V_i)/\sum_i \Delta V_i$, where ΔV_i is the volume of the grid cells, is much lower (figure 20, solid line). The difference is primarily related to the averaging procedure, since the formula applied takes into account each cell contribution in temperature linearly, whereas the contribution of each cell to the second ion lines decreases

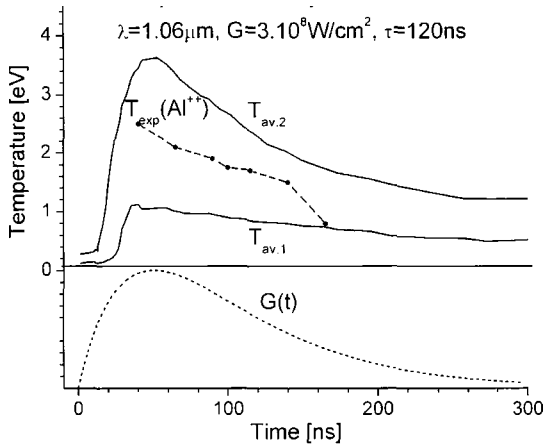

Figure 20. Comparison of plasma temperatures determined experimentally [59] $T_{\exp}(Al^{++})$ and predicted numerically at the same laser action parameters $T_{av.1}(t)$ (averaged over the plasma pattern), $T_{av.2}(t)$ (averaged along the beam axis). The dotted line denotes the temporal dependence of the laser intensity $G(t)$.

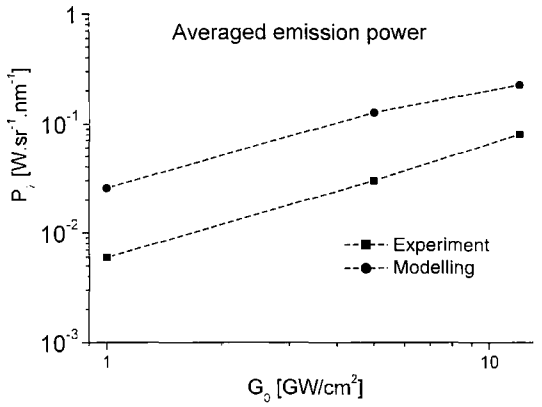

Figure 21. Average power emitted by the plasma into a specified solid angle in the spectral range $\Delta\lambda = 693$–697 nm determined experimentally [60] and predicted numerically at the following laser parameters: $\lambda = 1.06\,\mu$m, $\tau = 20$ ns, $G = 10^9$, 5×10^9 and 1.2×10^{10} W cm^{-2}.

much faster as the temperature decreases. On the other hand, the temperature curve $T_{av.2}(t)$, as determined by averaging along the plasma axis $z = 0$, majorizes the experimental curve from above (figure 20).

In [60] the action of the Nd–YAG laser with $\lambda = 1.06\,\mu$m and pulse duration $\tau = 20$ ns, at intensities of $(0.1$–$12) \times 10^9$ W cm^{-2} on the Al target in a medium at normal pressure was considered. A photodetector placed at an angle of 45° to the beam axis recorded the average intensity of radiation emitted in the solid angle of 1.3×10^{-4} sr within the spectral range 693–697 nm. The same quantity was computed for $G_0 = 10^9$, 5×10^9 and 1.2×10^{10} W cm^{-2} (figure 21). One can see in the figure that the computed values are several times greater than the experimental ones but are characterized by almost the same dependence on the intensity. The reasons for deviation are supposed to be the different setups of the physical and computational experiments and, in particular, due to the attenuation of the radiation as it is propagated from the plasma cloud to the detector as well as due to errors in predicting the angular dependence of the radiation field introduced by the DA.

The collection of experimental data on the temperature of laser-induced erosion plasmas for different target materials and laser wavelengths is presented in [38, p 36]. According to the data the temperature of plasma generated by laser radiation with the wavelength of $1.06\,\mu$m rises from 10 eV at $G = 10^9$ W cm^{-2} to 20–25 eV at $G = 2 \times 10^{10}$ W cm^{-2}. Coincidence with the results in figure 11 is rather good.

In the last few years the majority of studies of laser-induced plasmas is devoted to pulsed laser deposition (PLD) techniques, that utilize UV laser radiation with the intensity of 10^8–10^9 W cm^{-2}. The generated plasmas are relatively cold, $T_{\text{plasma}} = 2$–3 eV [61] and partially transparent for laser radiation. In [62], the optical properties of Al plasma created by the XeCl laser, $\lambda = 0.308\,\mu$m, $G = 10^9$ W cm^{-2}, $\tau = 30$ ns were studied and the typical optical thickness of the plasma was estimated to be 0.23. It means that intensive laser heating and evaporation of the target surface will continue after the plasma formation. In this case, the heat transfer, the phase transformations of the target and the processes in the plasma become closely coupled. Thus, the initial hot layer approximation that is valid and effective for modelling of opaque plasmas under the condition that the major part of target material evaporates before plasma formation, is inadequate for PLD plasma modelling.

5. Conclusion

The performed modelling of gas dynamical expansion and radiation transfer of Al vapour plasma under the action of a nanosecond laser allowed us to conclude the following:

(1) Radiation transfer significantly affects the plasma evolution when the intensity is greater than 10^9 W cm^{-2}. As the intensity rises the radiative energy losses increase and reach 60% at 2×10^{10} W cm^{-2}, causing a proportional reduction of the plasma temperature whose typical values are 10–20 eV. The energy escapes largely through the side boundary and to a smaller extent through the front boundary, the amount of energy escaping in the direction of the target being negligible.

(2) At fixed laser intensity the most intensive energy release, the highest temperature and the maximum value of radiative losses are observed for the action of the IR range at $1.06\,\mu$m. The dependence of the processes occurring in the plasma on the laser wavelength is due to the mechanisms of absorption. As the wavelength decreases from 1.06 to 0.532 and $0.248\,\mu$m (increase in the quantum energy) the photo-absorption processes become energetically allowed. At a relatively moderate temperature ($T \sim 1$ eV) their contribution is 1–4 orders greater than the inverse bremsstrahlung absorption, therefore at the stage of initial heating the plasma absorbs the short wave radiation more intensively. As the temperature rises ($T \sim 5$ eV) due to changes in the plasma charge composition the principal absorption mechanism is the inverse bremsstrahlung effect, whose coefficient decreases proportionally to the third power of the wavelength.

(3) The spectral composition of escaping radiation differs much from the Planck equilibrium distribution and is typical of plasma with a variable optical density. It is possible to take into account the effect of radiation transfer on the plasma characteristics by solving the equation for radiative

transfer within the multi-group approximation with 30–50 spectral groups covering the spectral range with the upper limit $h\nu_{max} \sim 10$ T.

(4) By using the maximum available number of groups for selected spectrum intervals (determined by the available data on the plasma absorption coefficient) the model allows us to qualitatively analyse the spectral composition of the escaping radiation (for example, appearance/disappearance of particular lines, the relation of their intensities) and to calculate the total value of radiative losses over the given spectral range. This makes it possible to obtain computed information to be compared with experimental data of laser emission spectroscopy.

References

[1] Anisimiv S I, Imas F Ya and Romanov G S 1970 *Dejstvije izluchenija bolshoj moshchnosti na metali* (Moscow: Nauka)

[2] Raizer Yu P 1977 *Laser-Induced Discharge Phenomena* (New York: Consultant Bureau)

[3] Weyl G, Pirri A and Root R 1981 *AIAA J.* **19** 460

[4] Mazhukin V I, Uglov A A and Chetverushkin B N 1981 *Dokl. Acad. Nauk SSSR* **256** 1100

[5] Von Allmen 1987 *Laser-Beam Interactions with Materials* (Berlin: Springer)

[6] Phipps C and Dreyfus R 1993 *Laser Microprobe Mass Analysis* ed A Vertes *et al* (New York: Wiley)

[7] Duley W W 1996 *UV Lasers: Effects and Applications in Material Science* (Cambridge: Cambridge University Press)

[8] Zeldovich Ya B and Raizer Yu P 1967 *Physics of Shock Waves and High Temperature Hydrodynamics Phenomena* vol I (New York: Academic)

[9] Bridges J M, Cromer C L and Mcllrath Th 1986 *J. Appl. Opt.* **25** 2208

[10] Hermann J, Boulmer-Leborgne C, Dubreuil B and Mihailescu I N 1993 *J. Appl. Phys.* **74** 3071

[11] Gizzi L A *et al* 1994 *Phys. Rev.* E **49** 5628

[12] Malama Yu G and Marchenko V S 1985 *Sov. J. Plasma Phys.* **11** 1181

[13] Bergelson V I and Nemtchinov I V 1978 *Sov. J. Quantum Electron.* **8** 1198

[14] Bergelson V I and Nemtchinov I V 1980 *Sov. J. Quantum Electron.* **10** 1373

[15] Martinenko O G, Pavlyukevich N V, Romanov G S and Soloukhin R I 1986 *Int. J. Heat Mass Transfer* **29** 1203

[16] Kokora A N, Romanov G S, Stankevich Yu A and Uglov A A 1987 *Zh. Fiz. Him. Obrabotki Materialov* **8** 54

[17] Mazhukin V I, Smurov I and Flamant G 1994 *J. Comput. Phys.* **112** 78

[18] Weyl G J 1994 *Thermophys. Heat Transfer* **8** 229

[19] Ho J R, Grogoropoulos C P and Humphrey J A C 1996 *J. Appl. Phys.* **79** 7205

[20] Mazhukin V I, Nossov V V and Smurov I 2001 *J. Appl. Phys.* **90** 607

[21] Erpelding A, Minardi P J and Bishop 1991 *J. Heat Transfer* **113** 939

[22] Xu X and Song K H 1997 *Trans. ACME* **119** 502

[23] Callies G, Schittenchelm H, Berger P, Dausinger F and Hugel H 1994 *SPIE Proc.* **2246** 126

[24] Modest M 1993 *Radiative Heat Transfer* (New York: McGraw-Hill)

[25] Romanov G S, Stankevich Yu A, Stankevich L K and Stepanov K L 1995 *Int. J. Heat Mass Transfer* **38** 545

[26] Romanov G S, Stepanov K L and Sirkin M I 1982 *Sov. J. Opt. Spectrosc.* **53** 381

[27] Taine J and Soufiani A 1999 *J. Adv. Heat Transfer* **33** 295

[28] Soloukhin P I (ed) 1984 *Radiacionnij teploperenos v visokotemperaturnich gazach* (Moscow: Energoatomizdat)

[29] Bazilev B N *et al* 1994 *Sov. Phys.—JETP* **106** 1628

[30] Singh R K and Narayan J 1990 *Phys. Rev.* B **41** 8843

[31] Aden M, Beyer E, Herziger G and Kunze H 1993 *J. Phys. D: Appl. Phys.* **25** 1545

[32] Vertes A, Dreyfus R W and Platt D E 1994 *IBM J. Res. Dev.* **38** 1

[33] Schittenchelm H, Callies G, Berger P and Hugel H 1996 *J. Phys. D: Appl. Phys.* **29** 1564

[34] Schittenchelm H, Callies G, Berger P and Hügel H 1998 *J. Phys. D: Appl. Phys.* **31** 418

[35] Rosen D I, Mitteldorf J, Kothandaraman G, Pirri A N and Pugh E R 1982 *J. Appl. Phys.* **53** 3190

[36] Popov A M, Popovicheva O B and Rakhimova T V 1988 *Sov. Phys.—Tech. Phys.* **14** 370

[37] Mazhukin V I, Nossov V V, Nickiforov M G and Smurov I 2003 *J. Appl. Phys.* **93** 56

[38] Gorbunoff A 2002 *Laser-Assisted Synthesis of Nanostructured Materials* Fortschritt-Berichte VDI Reich 9 Nr 357 (Dusseldorf: VDI Verlag)

[39] Chetveruskin B N 1992 *Dynamica izluchayuchego gaza* (Moscow: Nauka)

[40] Bushman A V and Fortov V E 1983 *Sov. J. Usp. Fiz. Nauk* **140** 177

[41] Kalitkin N N, Kuzmina L V and Rogov V S 1972 *Preprint* #2 IPM AN SSSR

[42] Nickiforov A F, Novikov V G and Uvarov V B 2002 *Quantum–Statistical Models of High-Temperature Plasma, Computations of Rosseland Free Runs and The Equations of State* (Moscow: Fizmatlit)

[43] Richter J 1968 *Plasma Diagnostics* ed W Lochte-Holtgreven (Amsterdam: North-Holland)

[44] Hartree D R 1957 *The Calculation of Atomic Structures* (New York: Plenum)

[45] Moore Ch 1949 *Atomic Energy Levels* vol I (Washington, DC: NBS)

[46] Wiese W L, Smith M W and Glennon B M 1966 *Atomic Transition Probabilities* vol I (Washington, DC: NSRDS)

[47] Griem H R 1974 *Spectral Line Broadening by Plasmas* (New York: Academic)

[48] Derjiev V I, Zhidkov A G and Yakovlenko S I 1986 *Radiation of Ions in Nonequilibrium Dense Plasma* (Moscow: Energoatomizdat)

[49] Vainshtein L A, Sobelman I I and Yukov E A 1979 *Excitation of Atoms and Spectral Line Broadening* (Moscow: Energoatomizdat)

[50] Fabbro R, Peyre P, Berthe L, Sollier A and Bartnicki E 2000 *Proc. SPIE* **3888** 155

[51] Gupta P D and Kumbhare S R 1984 *J. Appl. Phys.* **55** 1201

[52] Shirsat T S, Parab H D and Pant H C 1989 *Laser Particle Beams* **7** 795

[53] Devjyatich G G, Gaponov S V, Kovalev I D, Larin N V, Luchin V I, Maximov G A, Pontus L I and Shirkov A I 1976 *Sov. Tech. Phys. Lett.* **2** 136

[54] Mazhukin V I and Samarskii A A 1994 *Surveys Math. Industry* **4** 85

[55] Crout D 1936 *J. Math. Phys.* **15** 1

[56] Boyd I W 1987 *Laser Processing of Thin Films and Microstructures* (Berlin: Springer)

[57] Olson G L, Auer L H and Hall M L 2000 *J. Quant. Spectrosc. Radiat. Transfer* **64** 619

[58] Morel J E 2000 *J. Quant. Spectrosc. Radiat. Transfer* **65** 769

[59] Lenk A, Witke Th and Granse G 1996 *J. Appl. Surf. Sci.* **96–98** 195

[60] Chumakov A N, Min'ko L Ya and Smurov I 2000 Radiative properties of laser-induced plasmas in visible and UV spectral range private communication

[61] Gaidarenko D V, Leonov A G and Cherkov D I 1991 *Sov. J. Plasma Phys.* **17** 534

[62] Ageev V P, Gorbunov A A and Konov V I 1989 *Sov. J. Quantum Electron.* **19** 785